Hindawi
Geofluids
Volume 2024, Article ID 5515938, 17 pages
https://doi.org/10.1155/2024/5515938

*Research Article*

# A Two-Dimensional Planar Fracture Network Model for Broken Rock Mass Based on Packer Test and Fractal Dimension

**Lei Wen**,[1] **Ping Guo**,[1] **Xin Zhang**,[1] **Wen-qiang Lu**,[2] **and Zhong Fang Liu**[1]

[1]*School of Architectural Engineering, Chongqing Industry Polytechnic College, Chongqing 401120, China*
[2]*Chongqing Institute of Green and Intelligent, Technology Chinese Academy of Science, Chongqing 400722, China*

Correspondence should be addressed to Lei Wen; 821149277@qq.com and Wen-qiang Lu; wqlu@cigit.ac.cn

Received 5 September 2023; Revised 5 December 2023; Accepted 29 January 2024; Published 19 February 2024

Academic Editor: Bailu Teng



Broken rock masses with the complexity and concealment widely exist in nature such as underground mine, collapse column, and zone. It is extremely difficult to model fracture networks and to simulate water diffusion for broken rock masses. To explore a reasonable fracture network model for broken rock masses, a new method for modeling a two-dimensional planar fracture network model is proposed in this paper. It includes packer test, empirical relationship, fractal width description, and symmetric expansion modeling. Then, the fluid-solid coupling is used to simulate the diffusion properties of water in the two-dimensional planar fracture network model. It is found that the diffusion velocities $v_{\max}$ and $v_{\min}$ do not appear in the fracture widths $\lambda_{\max}$ and $\lambda_{\min}$. It indicates that the fracture widths $\lambda_{\max}$ and $\lambda_{\min}$ in the fracture network model for broken rock mass have little impact on the diffusion velocity. Furthermore, the fracture distribution pattern in the fracture network model is an important factor affecting the diffusion velocities $v_{\max}$ and $v_{\min}$. The simulation results of water diffusion in the currently proposed model are almost consistent with the actual process of the packer test. Also, the validity of the two-dimensional planar fracture network model is verified by comparing the simulation results with the existing research.

## 1. Introduction

Severe accidents in construction periods, such as collapses and landslides, are easily caused by broken rock masses, severely threatening engineering safety. Grouting is one of the most common and effective methods for reinforcing broken rock masses. The grouting technique and grouting material are crucial factors for determining the grouting reinforcement effects [1–4]. However, the concealment of grouting objects challenges the verification and evaluation of the grouting reinforcement effect. Thus, various methods, such as laboratory tests, field tests, and numerical simulations, are used to study the grouting reinforcement effect and the diffusion range of grouting fluid.

Fractured rock exists widely in geological engineering, such as in collapse zones, collapse columns, and underground mines. Randomly distributed existing fractures have a negligible effect on seepage characteristics [5, 6]. In particular, the randomly distributed fractures in a broken rock mass dominate the diffusion characteristics. In this respect, Alireza and Tayfun [7] proposed a correlation to predict the effective fracture network permeabilities for natural fracture. The effective fracture network permeability is based on 2-dimensional fracture. For fractal dimensions, the scanning line and intersection points of the natural fracture are two critical factors but ignoring fracture width. These randomly distributed fractured areas form a connected fracture network in a two-dimensional plane, which provides the motivation to study fracture networks in two dimensions, as in this work.

Fractures in rocks are disordered, showing statistically self-similar and fractal characteristics [8–13]. Torabi and Berg [14] stated in their comprehensive review the scaling laws on length distributions. Also, Velde et al. [15] and Vignes-Adler et al. [16] concluded that the distribution of rock fractures can be characterized by fractal dimension. Therefore, it is reasonable to use fractal dimension to show the characteristics of rock mass fractures. Besides, Wang et al. [17] established a fractal model according to a relationship between the macrostructural parameters and microstructural parameters of a fracture network. The proposed fractal model for the Bingham fluids concluded that the initial pressure gradient decreases with increasing porosity of matrix material, fractal dimension for mother diameters, and permeability. Their research hints that the initial pressure gradient of the proposed fractal model is determined by macroscopic structural parameters. Likewise, Zheng and Yu [18] investigated gas diffusion characteristics of porous media using randomly distributed fractal-like tree networks in the matrices. They proposed that the gas permeability is a function of structural parameters of dual-porosity media, which does not contain any empirical coefficients. In particular, Miao et al. [19] proposed a fractal-based model that is a function of the fractal dimension $D$ for a broken rock mass. In Miao et al.'s research, the fractal dimension $D$ is determined by many factors, such as fracture area, area porosity, fracture density, the maximum fracture length, aperture, the facture azimuth, and facture dip angle, and their model validated the available numerical simulations.

Moreover, experimental analyses and numerical simulations of the grouting reinforcement for broken rock masses have been presented by some researchers [20–24]. Lange and Van Geel [25] constructed a new experimental model to analyze and evaluate the effectiveness of the fluid pressure gradient and mass flux in a surrounding rock mass with two fractures. Nishimura et al. [26] studied microgrouting technology. Their research results show that the stress changes depend on the depth and the interaction between adjacent grouting piles, which provides a research idea for grouting stress coupling simulation in the current paper. Du et al. [27] analyzed the variations of the pressure characteristics during the grouting process by simulating the compression grouting process in a geotechnical centrifuge. The sealing efficiency increases with high fractal dimension while near the grouting source. Conversely, the sealing efficiency decreases with low fractal dimension. Kvartsberg and Fransson [28] constructed a model of a set of random water-conducting fissures according to hard rock test data and the characteristics of water-conducting fissures. They analyzed the diffusion characteristics of grouting fluid through numerical simulation. Zhou et al. [29] established a mechanical model of the interaction between a fully grouted bolt and the surrounding rock. They proposed a numerical simulation analysis of the fully grouted bolt considering the multiple yield conditions of the anchor element. These studies verified the effectiveness and reliability of the numerical simulation method through static experiments of grouted bolts.

Numerical simulation can be seen as an auxiliary method with which to effectively study grouting reinforcement. In the existing numerical simulation methods of grouting reinforcement, a geometric model is constructed by setting the permeability rate of the medium. Lei et al. [30] proposed a hybrid finite-discrete element model to simulate and analyze fluid flow in fractured geological media. In their hybrid finite-discrete element model, the simulation of fluid flow in fractured rocks is performed in an equivalent permeability. Wang et al. [17] proposed that stochastic fracture network model can be used to estimate hydraulic conductivity tensor for fractured rocks and to simulate fluid flow.

However, the geometric models constructed in above way can hardly be effectively verified by using rock engineering. The spatial distribution and shape of fractures in rock masses have great uncertainty and particularity, mainly due to irregular fracture terminations. The complexity and concealment of broken rock masses causes a bottleneck in the construction of a reasonable geometric model. Therefore, building a reasonable geometric model of a broken rock mass is critical for simulating the flow and diffusion of the grouting fluid. Especially for solving engineering problems, the accuracy of geometric models is more important. According to packer test data and existing empirical relationship, a new method for constructing the geometric model of a broken rock mass is proposed in this study. The fractal dimension in the currently new method is carried out in using the maximum and minimum fracture widths. Finally, the constructed geometric model is realized by numerical simulation, and the simulation results are in good agreement with the existing research.

## 2. Packer Test

*2.1. Engineering Background.* A specific range of sliding fracture zones was exposed in an underground mine of the Fankou Lead-Zinc Mine due to collapse [24]. Fankou Lead-Zinc Mine is an underground mine located in Shaoguan City, Guangdong Province, China. Because of poor geological conditions, the mine adopts the room and pillar method to mine lead-zinc ore at intervals through blasting. The engineering background in detail was stated by Wen et al.'s research [24]. Due to unreasonable excavation sequence and untimely filling, as a result, the filling body on both sides of 0# stope slides to the 0# goaf and the roof of the 0# stope collapses. The collapse range and slip area are shown in Figure 1.

In Figure 1, the black-dotted line is the slip line detected according to the borehole investigation. The magenta color represents the slip line obtained from the numerical simulation analysis. The direction of the red arrow is the slip direction; that is, the filling body on both sides of 0# stope filled the previously empty area of the stope. The scope of the collapse area and the approximate slip surface position is preliminarily predicted through drilling and numerical simulation analysis, as shown in Figure 2. The numerical simulation analysis of the mining area shows that the strain in the slipped fracture zone is quite different. Moreover, according to the field drilling and coring results, the rock mass near the slip surface is broken, and there is no intact core, as shown in Figure 3.

*2.2. Packer Test.* To enhance the bearing capacity and stability of the slip zone, grouting reinforcement must be carried out in this area. How can the diffusion range of grouting be determined? Numerical simulation provides an effective method for the flow and diffusion of grouting fluid. For a fractured rock mass, the key of this study is how to build a geometric model for the broken rock mass with a slip zone using numerical simulation. Before grouting reinforcement in this area, a packer test is carried out to obtain the

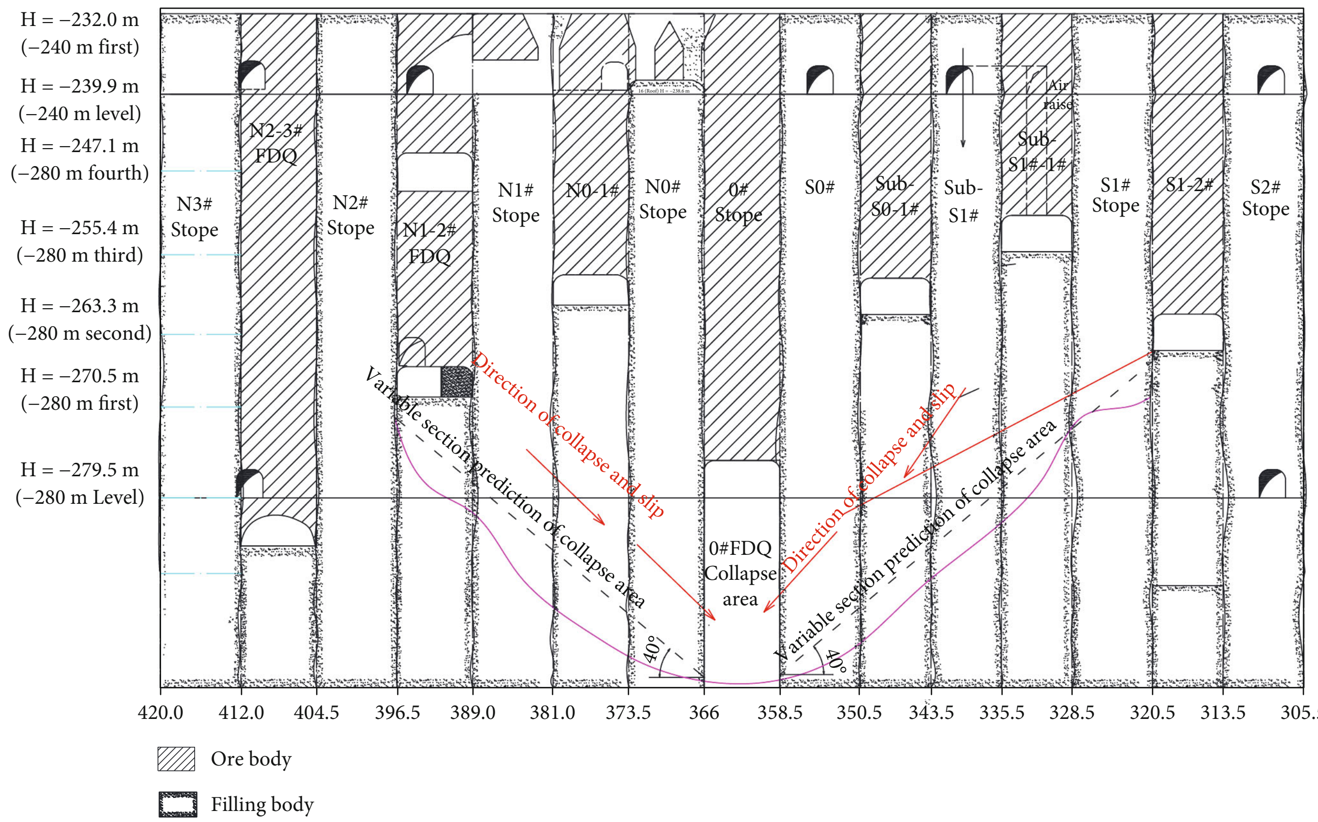


Figure 1: Scope of the collapse area.

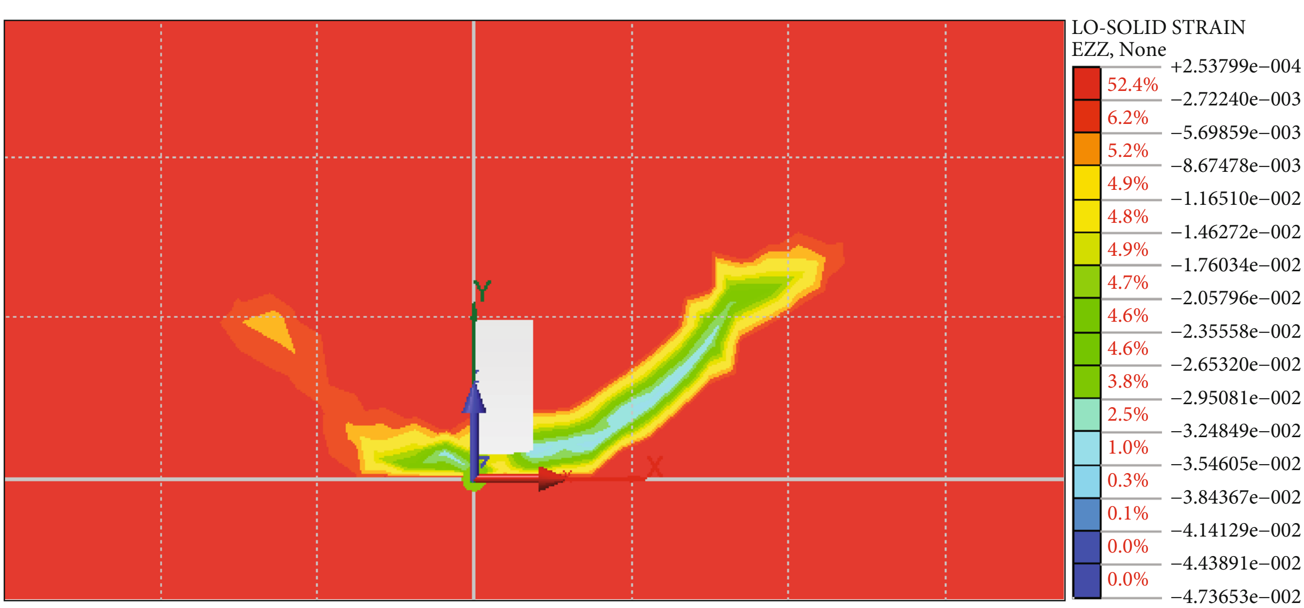


Figure 2: $z$ direction strain contour plot of the slip surface in the collapse area.

permeability rate of the broken rock mass. More importantly, the packer test also provides an essential basis for building the geometric model of numerical simulation.

The packer test is an in situ test [31]. The water is injected into the borehole at the high pressure to understand the fracture development and permeability of the rock mass according to the calculation of water absorption. Also, the packer test is a method frequently used to evaluate and judge the permeability of rock masses. In this study, the packer test is carried out to measure the permeability rate of the broken rock mass. The packer test is divided into two main stages.

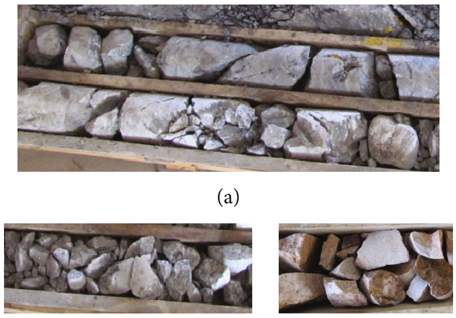
(a)
(b) (c)

Figure 3: Broken drill cores ((a–c) the rock cores of different boreholes).

The first stage is called the pretest stage, which is necessary to set the test pressure. Then, the initial pressure slowly increases to the set test pressure and is maintained for 30 minutes. In the case of a pressure drop during the initial pressure increases, supplementary pressure is needed, but the extra pressure shall not exceed the test pressure. Meanwhile, it is necessary to check whether there is water leakage at the pipe interface and accessories.

The next stage is the primary test stage. When the pressure reaches the test pressure, the water injection is stopped and maintained for 15 minutes. If the pressure drop is within the allowable threshold range and remains constant for 30 minutes and there is no water leakage, the packer test is deemed to be successful.

The test length of the packer test hole in this study is 8 m, and the test pressure is 0.8 MPa. A schematic diagram of the packer test device is shown in Figure 4. After the water blocking plug reaches the predetermined hole position, the water plug is tested with the maximum pressure to detect water leakage. Then, the pressure gauge and flow meter data are recorded simultaneously. The reading on the pressure gauge is recorded once every 10 minutes, and the pressure is kept stable. The flow test results must meet the following conditions:

(1) For four consecutive records, the differences between maximum and minimum values are less than 10% of the minimum final values
(2) When the flow decreases gradually, the recorded values for four consecutive times are less than 0.5 L/min
(3) When the flow increases gradually, there is no increasing trend for four consecutive records

The results of the packer test are expressed as unit water absorption, that is, water permeability, which is described as follows:

$$q = \frac{Q_0}{L_0 P_0}, \quad (1)$$

where $q$ is the permeable rate (Lu), $Q_0$ is the flow per unit time (L/min), $L_0$ is the length of the packer test section (m), and $P_0$ is the tested pressure (MPa).

As shown in Figure 4, the low-pressure water at 0.8 MPa is injected into the test hole at 0.8 MPa. When water overflows from the outlet hole, the water pump stops working and records the injected water volume, and the water pressure of the outlet hole is regarded as 0 MPa. The test results are listed in Table 1. The results of RQD value indicate that the rock mass in study area is extremely broken.

## 3. Plane Model Construction Scheme of a Broken Rock Mass

The packer test in the broken rock mass is carried out to measure the permeability rate. According to the existing experimental research, an empirical relationship between the osmotic coefficient and fractal dimension was established by Wu [32]. Thus, the fractal dimension of the broken rock mass is used to build an equivalent fracture model. The constructed model is used to analyze the simulated water flow characteristics and diffusion range. The reliability of the model is determined by performing the numerical simulation. The construction and validation framework of the current model is shown in Figure 5.

*3.1. Fractal Theory of a Fractured Rock Mass.* Randomly distributed fractures with irregular sizes are common in rock masses. The existing research concluded that the fractured rock masses show fractal characteristics [33–35]. Thus, the fractal dimension is used to quantitatively characterize the fracture characteristics of a fractured rock mass, which provides a credible research basis for establishing a geometric model consistent with the rock structure observed in field practice.

For the fractal dimension of the broken rock mass, there are two hypotheses as follows:

(1) The fractures of the broken rock mass are connected in the three-dimensional space
(2) The distribution and scale of fractures in-plane or in the three-dimensional space fit the fractal scale

In the study area, one area is regarded as a representative unit area (RUA). The relationship between the cumulative number of fractures and the plane width of fractures in the RUA can be expressed with the following [19, 36].

$$N(L \geq \lambda) = \left(\frac{\lambda_{\max}}{\lambda}\right)^{D_{\mathrm{f}}}, \quad (2)$$

where $L$ represents the fracture length, $\lambda$ represents a threshold fracture length, $N$ represents the total number of fractures with a length greater than or equal to $\lambda$, $\lambda_{\max}$ represents the maximum value of fracture length in the RUA, and $D_{\mathrm{f}}$ represents the fractal dimension of the fracture length ($\lambda$) distribution. The $D_{\mathrm{f}}$ value indicates the uniformity of the fracture length. That is, the greater the value of $D_{\mathrm{f}}$ is, the worse the uniformity. The $D_{\mathrm{f}}$ fluctuates from 0 to 2 in the two-dimensional plane space. In the three-dimensional space, the value range is expressed as 0 to 3.

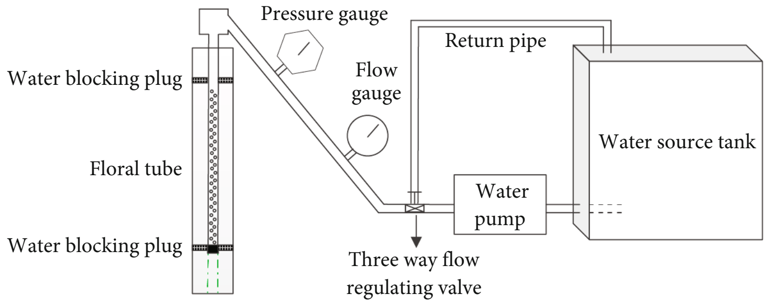


Figure 4: Packer test device diagram.

Table 1: The test results of packer test.

| No. | Deep (m) | RQD value (%) | Injection pressure (MPa) | Interval between water inlet and water outlet (m) | Permeable rate (Lu) |
|---|---|---|---|---|---|
| 637-YK1 | 9.5 | 45.2 | 0.816 | 8.1 | 115.6 |
| 649-YK1 | 8.9 | 39.7 | 0.796 | 7.9 | 116.7 |
| 657-YK1 | 9.3 | 41.8 | 0.793 | 8.3 | 113.1 |
| 667-YK1 | 9.6 | 46.3 | 0.80 | 8.1 | 116.2 |
| 673-YK1 | 9.1 | 53.1 | 0.802 | 8.1 | 113.4 |

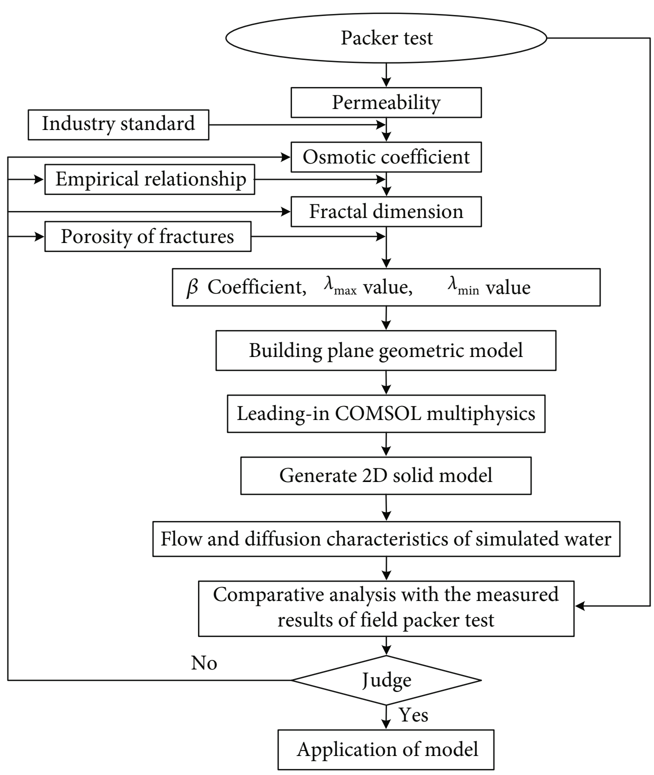


Figure 5: The construction and validation framework of the current model.

After differentiating $\lambda$ in Eq. (2), $D_f$ can be expressed as shown in the following:

$$-dN(\lambda) = D_f \lambda_{\max}^{D_f} \lambda^{-(D_f+1)} d\lambda. \quad (3)$$

In porous media, Yu and Li [36] proposed a unified model, as shown in the following:

$$D_f = d_e + \frac{\ln \varepsilon}{\ln (r_{\max}/r_{\min})}, \quad (4)$$

where $\varepsilon$ is the effective porosity and the ratio $(r_{\mathrm{max}}/r_{\mathrm{min}})$ is derived from an assumption that the pores are regarded as the form of squares that are self-similar in terms of sizes [36]. However, it is redefined in Miao et al.'s [19] research that $r_{\mathrm{min}}$ represents the minimum value of fracture lengths, $r_{\mathrm{max}}$ represents the maximum value of fracture lengths, $d_{\mathrm{e}}$ is the Euclidian dimension, $d_{\mathrm{e}}$ is 2 in two dimensions, and $d_{\mathrm{e}}$ is 3 in three dimensions.

Fractures in broken rock masses can be regarded as pores. As an originality of the paper, the fracture lengths $r_{\mathrm{min}}$ and $r_{\mathrm{max}}$ in Eq. (4) is refined by fracture widths $\lambda_{\mathrm{min}}$ and $\lambda_{\mathrm{max}}$. Thus, Eq. (4) is also applicable to fracture in a rock mass. Eq. (4) can be rewritten as

$$D_{\mathrm{f}} = d_{\mathrm{e}} + \frac{\ln \phi_{\mathrm{c}}}{\ln \left(\lambda_{\mathrm{max}}/\lambda_{\mathrm{min}}\right)}, \quad (5)$$

where $\phi_{\mathrm{c}}$ represents the effective porosity of fractures in a rock mass, which is a ratio of the projected area of the fractures in the RUA to the total projected area of the RUA.

According to Eq. (3), the projected area $A_{0\mathrm{p}}$ of fractures in the RUA can be expressed as

$$A_{0\mathrm{p}} = -\int_{\lambda_{\mathrm{min}}}^{\lambda_{\mathrm{max}}} a \cdot \lambda \cdot dN(\lambda) = \frac{\beta D_{\mathrm{f}} \lambda_{\mathrm{max}}^{2}}{\left(d_{\mathrm{e}} - D_{\mathrm{f}}\right)} \left[1 - \left(\frac{\lambda_{\mathrm{min}}}{\lambda_{\mathrm{max}}}\right)^{d_{\mathrm{e}}-D_{\mathrm{f}}}\right], \quad (6)$$

where $a$ is the effective width of the rupture and $\beta$ is a ratio of $a$ to $\lambda$ [14, 35].

The plane projection of fractures in the broken rock mass can be regarded as complete connectivity in the two-dimensional plane model. Therefore, Miao et al. [19] had proposed that the porosity $\phi_{\mathrm{a}}$ of fractures can be redefined with the following:

$$\phi_{\mathrm{a}} = \frac{A_{0\mathrm{p}}}{A_{0}} = \frac{\beta D_{\mathrm{f}} \lambda_{\mathrm{max}}^{2}}{A_{0}\left(d_{\mathrm{e}} - D_{\mathrm{f}}\right)} \left[1 - \left(\frac{\lambda_{\mathrm{min}}}{\lambda_{\mathrm{max}}}\right)^{d_{\mathrm{e}}-D_{\mathrm{f}}}\right], \quad (7)$$

where $A_{0}$ represents the total area of the RUA.

Furthermore, based on Eq. (5), the porosity $\phi_{\mathrm{a}}$ of fractures can be expressed as

$$\phi_{\mathrm{a}} = \left(\frac{\lambda_{\mathrm{min}}}{\lambda_{\mathrm{max}}}\right)^{d_{\mathrm{e}}-D_{\mathrm{f}}}, \quad (8)$$

where $d_{\mathrm{e}} = 2$ (or 3) in two (or three) dimensions.

Since the fractured rock mass fractures are almost connected, the broken state of the three-dimensional fractured rock mass is also regarded as connected when projected to a two-dimensional plane. In this case, fracture width is the key factor affecting water flow diffusion in the packer test. In numerical simulation, for opening fracture, the fracture width is a crucial factor in the process of fluid diffusion, especially the Poiseuille flow of fluids in narrow opening fracture [37]. In this research, thus, the $\lambda_{\mathrm{max}}$ and $\lambda_{\mathrm{min}}$ in Eqs. (6)–(8) are regarded as the maximum and minimum fracture widths.

In this study, the porosity $\phi_{\mathrm{c}}$ of fractures is applied in the plane model. Therefore, $d_{\mathrm{e}} = 2$ is employed in Eq. (5). Also, we can obtain porosity based on Eq. (7) and Eq. (8). Then, the two-dimensional plane model of the broken rock mass is generated by setting the $\lambda_{\mathrm{max}}$ and $\lambda_{\mathrm{min}}$ values. In conclusion, it is feasible to establish a geometric model with a specific fracture porosity that is consistent with the fractal dimension.

### *3.2. Construction of a Two-Dimensional Model of a Broken Rock Block Mass*

*3.2.1. Empirical Relationship between the Fractal Dimension and Osmotic Coefficient.* According to a geometric model of the stable structure and an irregular fissure structure model, Wu [32] proposed an empirical relationship between the fractal dimension and osmotic coefficient. He also researched the correlation between the fractal dimension of actual fractures and permeability in the rock mass.

According to the existing experimental data [32], the empirical relationship between the osmotic coefficient $K$ and fractal dimension $D_{\mathrm{f}}$ is better fitted by a cubic polynomial, as shown in Figure 6. From Figure 6, we can obtain an empirical relationship between fractal dimension $D_{\mathrm{f}}$ and osmotic coefficient $K$, as shown in the following:

$$D_{\mathrm{f}} = -3.5832K^{3} + 3.2225K^{2} - 1.0922K + 1.8975. \quad (9)$$

According to the Technical Code for High-Pressure Jet Grouting of Water Conservancy and Hydropower Projects for China, the transformation relationship between permeable rate $q$ and the osmotic coefficient $K$ is given by

$$K = q \times 1.3 \times 10^{-5} \mathrm{cm/s}. \quad (10)$$

Figure 6 shows the results of the experimental data. Miao et al. [19] had derived the analytical relationship between fractal dimension and permeability based on the cubic law. In Figure 6, when the fractal dimension fluctuates between 1.76 and 1.90, the empirical relationship is good consistency with derived analytical model of Miao et al. [19].

*3.2.2. Construction of a Plane Model of the Broken Rock Mass.* All fractures in the broken rock mass are considered to be connected. For a section is selected in the study area of a broken rock mass, all fractures on the section are assumed to be connected. In these cases, the studied area of the broken rock mass is assumed to consist of countless sections. Then, the diffusion and flow of water in each section are approximately consistent.

Taking the water injection hole as the central axis, the water radially diffuses evenly in the periphery of the broken rock mass in a cylinder mode. The diffusion radius is uniformed, as shown in Figure 7. In the process of a packer test, the pore characteristics of the broken rock mass with water pressure holes are assumed to be centrosymmetric and consistent or similar.

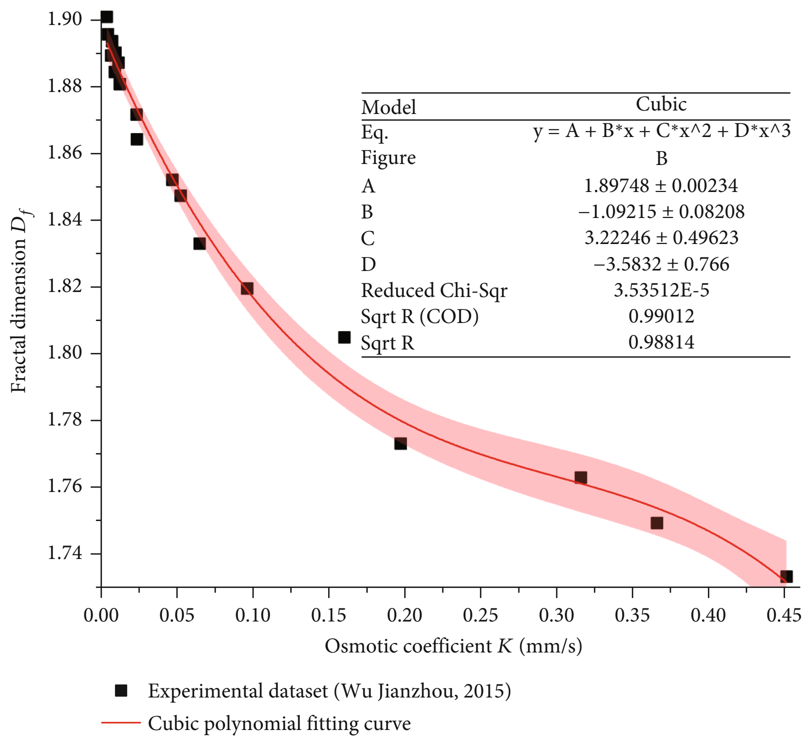


Figure 6: Fitting relationship between the fractal dimension and osmotic coefficient.

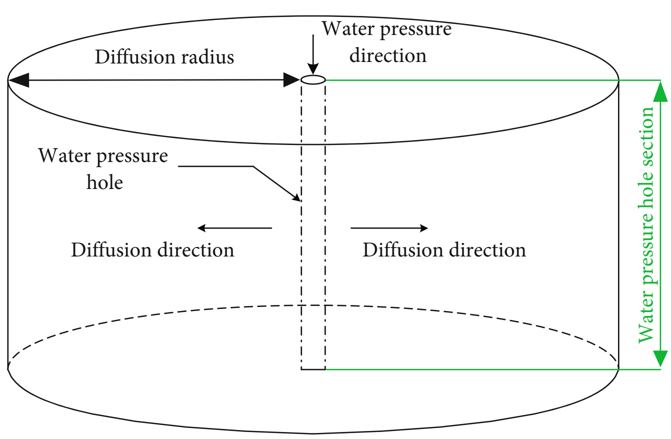


Figure 7: Schematic diagram of the cylindrical model for packer test diffusion.

Figure 7 supports the assumption that the water pressure on the borehole wall is uniform. The water pressure flowing from the hole wall into the broken rock mass is the test pressure. Additionally, the fractures of the broken rock mass are connected in the three-dimensional space, and they are also connected to project the connected fractures on the two-dimensional plane.

For the model of an irregularly broken rock mass, it is difficult to ensure that the fracture surfaces remain parallel. Thus, according to the statistical principle, the nonuniformity coefficient of the fracture is introduced into this simulation calculation, and its expression is as shown in the following:

$$c = \frac{\lambda_{\max} - \lambda_{\min}}{\bar{x} \times N}, \tag{11}$$

where $N$ represents the number of fractures in the RUA, $\bar{x}$ represents the average value of the fracture aperture, and $c$ represents the nonuniformity coefficient of the fracture, which is a ratio of the total fracture area to the fracture path length.

Since the nonuniformity coefficient reduces the connectivity of fractures, Eq. (7) is rewritten as

$$\phi_a = \frac{A_{0p}}{A_0} = c\frac{\beta D_f \lambda_{\max}^2}{A_0 (d_e - D_f)} \left[1 - \left(\frac{\lambda_{\min}}{\lambda_{\max}}\right)^{d_e - D_f}\right]. \tag{12}$$

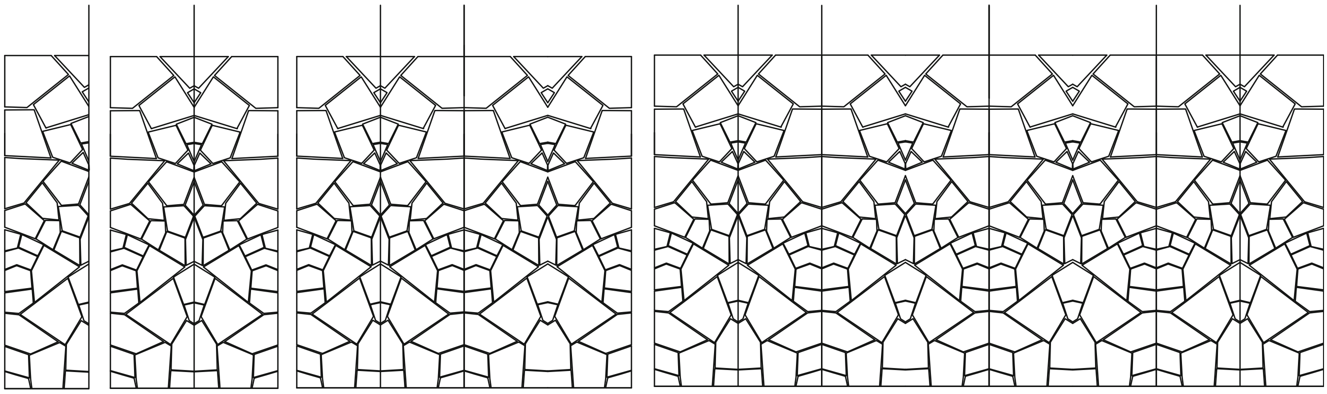


Figure 8: Geometric model of a two-dimensional plane of the in situ broken rock mass.

Table 2: Fracture parameters of the broken rock mass in the unit area. (a) Projected area of fractures per unit area. (b) Fracture trace length per unit area.

(a)

| No. | 1 | 2 | 3 | 4 | 5 | 6 | 7 | 8 | 9 | 10 | 11 | 12 |
|---|---|---|---|---|---|---|---|---|---|---|---|---|
| Projected area ($m^2$) | 0.0876 | 0.0218 | 0.0017 | 0.0585 | 0.063 | 0.0346 | 0.0111 | 0.0024 | 0.0052 | 0.0609 | 0.0469 | 0.0249 |
| No. | 13 | 14 | 15 | 16 | 17 | 18 | 19 | 20 | 21 | 22 | 23 | 24 |
| Projected area ($m^2$) | 0.0055 | 0.0241 | 0.0318 | 0.0166 | 0.0107 | 0.0199 | 0.0103 | 0.009 | 0.0103 | 0.0178 | 0.0206 | 0.0484 |
| No. | 25 | 26 | 27 | 28 | 29 | 30 | 31 | 32 | 33 | 34 | Total | |
| Projected area ($m^2$) | 0.0198 | 0.0198 | 0.0733 | 0.0049 | 0.0462 | 0.0338 | 0.0205 | 0.0119 | 0.0494 | 0.0147 | 0.9379 | |

(b)

| No. | 1 | 2 | 3 | 4 | 5 | 6 | 7 | 8 | 9 | 10 | 11 | 12 | 13 |
|---|---|---|---|---|---|---|---|---|---|---|---|---|---|
| Trace length (m) | 0.26 | 0.05 | 0.07 | 0.32 | 0.17 | 0.27 | 0.31 | 0.32 | 0.18 | 0.09 | 0.13 | 0.11 | 0.04 |
| No. | 14 | 15 | 16 | 17 | 18 | 19 | 20 | 21 | 22 | 23 | 24 | 25 | 26 |
| Trace length (m) | 0.33 | 0.12 | 0.18 | 0.1 | 0.17 | 0.08 | 0.15 | 0.09 | 0.15 | 0.11 | 0.12 | 0.11 | 0.17 |
| No. | 27 | 28 | 29 | 30 | 31 | 32 | 33 | 34 | 35 | 36 | 37 | 38 | 39 |
| Trace length (m) | 0.19 | 0.12 | 0.18 | 0.08 | 0.08 | 0.13 | 0.16 | 0.09 | 0.17 | 0.17 | 0.19 | 0.08 | 0.36 |
| No. | 40 | 41 | 42 | 43 | 44 | 45 | 46 | 47 | 48 | 49 | 50 | Total | |
| Trace length (m) | 0.15 | 0.25 | 0.05 | 0.32 | 0.2 | 0.15 | 0.4 | 0.26 | 0.14 | 0.15 | 0.03 | 8.3 | |

For the broken rock mass, the construction of a two-dimensional plane model meets the following assumptions:

(1) The distribution of fractures in the study area is approximately the same as that in the three-dimensional space. That is, the fractal dimension is the same

(2) The fracture scale accords with the fractal geometry feature. The fractures in a small area are nonuniform, but the whole area is approximately homogeneous

According to the physical meaning of the fracture porosity, the generation and extension of a two-dimensional geometric model of a broken rock mass are shown in Figure 8. The fracture parameters of the model unit in Figure 8 is listed in Table 2 (a) and (b). In particular, those data are the raw data of the model unit. Then, the model unit of Figure 8 is extended asymmetrically. The model unit of Figure 8 is magnified, as shown in Figure 9. Figure 9 shows the maximum and minimum fracture apertures. In the model unit, the area of fracture opening can be obtained as shown in the following:

$$s_c = s_a - s_r, \tag{13}$$

where $s_c$ is the area of the fracture opening, $s_a$ is the area of a model unit, and $s_r$ is the scope of the block in the model unit.

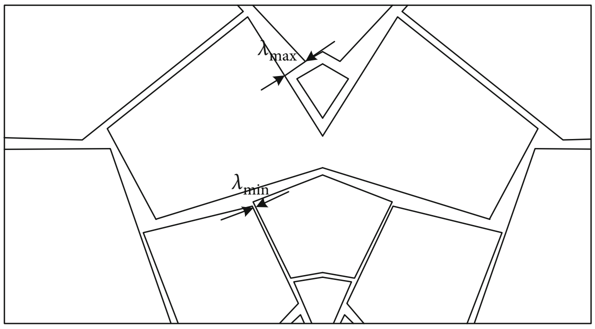


Figure 9: Plane geometric model of different $\lambda$ values in the local area.

The average value of the effective fracture aperture in the model unit can be expressed via

$$\bar{\lambda} = \frac{s_c}{L_a}, \tag{14}$$

where $\bar{\lambda}$ is the mean value of the fracture aperture and $L_a$ is the whole trace length of the fracture in the model unit.

## 4. Modeling and Simulation Analysis

On the basis of Yu's fractal dimension [19, 36] on fracture length, in this paper, the fracture width is used to express the fractal dimension for the opening fracture of broken rock mass. And the geometric model of the two-dimensional plane fracture network is generated. The procedures for generating the two-dimensional fracture network model are carried out in Section 3. First, the packer test of the broken rock mass is carried out. Second, the fractal dimension of the fractured rock mass is obtained according to the empirical relationship between the permeability rate and the fractal dimension. Of course, the maximum and minimum fracture widths are also placed in the model. Based on above parameters, the symmetrical expansion method is used to generate the plane model of an irregular fracture network of the broken rock mass. Finally, the procedure of the packer test is simulated in view of the established plane model. The processes of model generation are as follows:

(1) The permeability rate is obtained from the broken rock mass packer test

(2) The empirical relationships of Eq. (9) and Eq. (10) are employed to obtain the osmotic coefficient and fractal dimension

(3) Eqs. (6)–(8) are used to determine these fracture parameters, which are used to generate a geometric plane model

(4) Finally, the geometric plane model is imported into simulation software to simulate the water diffusion procedures

*4.1. Plane Fracture Model of Fractured Rock Mass.* The permeability measured by the field packer test is the primary parameter, and the fractal dimension, fracture degree, and $\lambda_{max}$ and $\lambda_{min}$ values are obtained according to Eqs. (6)–(8). In this regard, the two-dimensional plane model of a fracture network in the fractured rock mass is generated in numerical simulation software, as shown in Figure 10. Under constant initial pressure, the steady-state method is employed to simulate the flow state and diffusion range of water in the fracture model.

Two different fracture forms are shown in the current model. The fragmentation of the broken rock mass is considerable, the fractures formed are sparse, and the width of fractures is significantly larger. The other fracture form is that the fragmentation of broken rock is small, and the formed fractures are dense, but the fracture width is small.

The model size is determined according to the actual size of the field packer test. In the geometric model of Figure 10, the mean fracture width $\bar{\lambda}$ of the fracture width can be obtained by a ratio of the fracture area to the fracture trace length. The fracture area is different between the model area and the rock block area. AutoCAD can be used to compute the rock block area. In this model, the $\bar{\lambda}$ value is 7.5 mm, and the $\lambda_{max}$ and $\lambda_{min}$ values are listed in Table 3. The fractal dimension and $\bar{\lambda}$ value is constant, and the geometric model is constructed according to the actual size of Table 3.

A difference of fracture distribution exists between the current plane geometric model and the in situ broken rock mass of the packer test. Therefore, fluid boundary conditions are set symmetrically to ensure the dimensional consistency between the current plane geometric model and the fracture morphology of in situ broken rock mass. Figure 10 shows that the fluid boundary conditions include an inlet, outlet, and symmetrical boundary. The inlet boundary defines an initial water pressure of 0.8 MPa. The water pressure of the outlet boundary is 0 MPa. Additionally, the upper and lower boundaries of the model of Figure 10 are defined as symmetrical boundaries to save computational memory and improve computational efficiency. Furthermore, the definition of an asymmetrical boundary reduces the dimensional difference between the model and packer test scenarios.

*4.2. Fluid-Solid Coupling Model.* According to Newton's law of viscous fluid movement between plates [38], the shear stress in the $x$ direction of the surface of the fluid microelement (FME) can be expressed as

$$\tau_{xy} = \mu\left(\frac{\partial v_x}{\partial y} + \frac{\partial v_y}{\partial x}\right), \tag{15}$$

where $\tau_{xy}$ represents the shear stress in the $x$ direction of the FME, $\mu$ represents the viscosity of viscous fluid, and $v_x$ represents the flow rate in the $x$ direction. According to the reciprocal theorem of shear stress, it can be concluded $\tau_{xy} = \tau_{yx}$. Otherwise, the FME will accelerate its rotation. In fact, the rotation of the FME only occurs in the separation

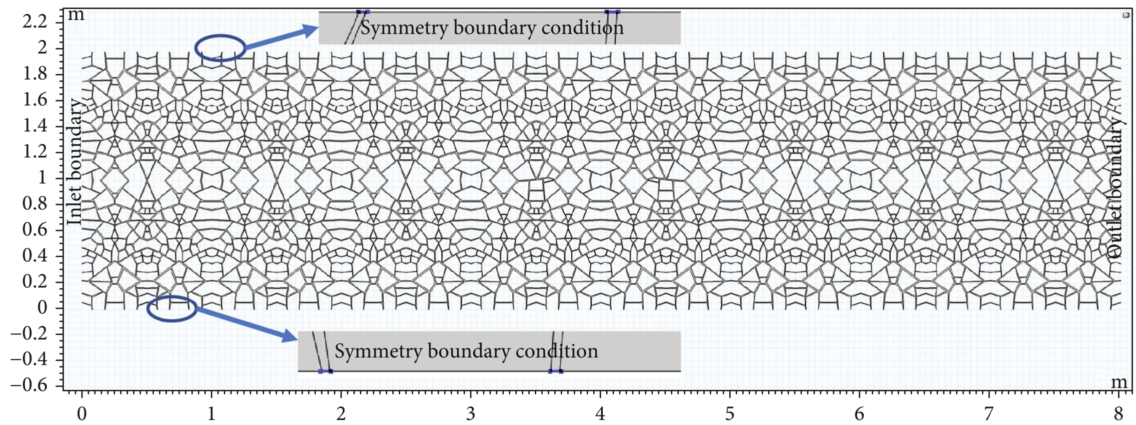


FIGURE 10: Geometric model of the two-dimensional planes of the fractured rock mass.

TABLE 3: Fracture parameters of the two-dimensional plane geometric modeling.

| Permeable rate (Lu) | Fractal dimension | No. | $\lambda_{max}$ | $\lambda_{min}$ | Fractured rate (%) | No. | $\lambda_{max}$ | $\lambda_{min}$ | Fractured rate (%) |
|---|---|---|---|---|---|---|---|---|---|
| | | A | 10 mm | 1 mm | 6.1654 | B | 9 mm | 1 mm | 5.6730 |
| 115 | 1.79 | C | 8 mm | 1 mm | 5.1690 | D | 7 mm | 1 mm | 4.6515 |
| | | E | 6 mm | 1 mm | 4.1182 | F | 5 mm | 1 mm | 3.5658 |

process of the boundary layer. Based on the above, the shear stress in $y$ direction and $z$ direction can also be expressed as

$$\begin{aligned}\tau_{yz} = \tau_{zy} = \mu\left(\frac{\partial v_y}{\partial z} + \frac{\partial v_z}{\partial y}\right),\\ \tau_{xz} = \tau_{zx} = \mu\left(\frac{\partial v_x}{\partial z} + \frac{\partial v_z}{\partial x}\right).\end{aligned} \tag{16}$$

Thus, the viscous force of the FME in the $x$ direction can be expressed as

$$f_x = \upsilon\nabla^2 v_x + \upsilon\frac{\partial}{\partial x}(\nabla\cdot\boldsymbol{v}) = \upsilon\nabla^2 v_x, \tag{17}$$

where $\upsilon$ is the ratio of $\mu$ to $\rho$. The continuity equation of incompressible fluid is $\nabla\cdot\boldsymbol{v} = 0$, where $\boldsymbol{v}$ is the velocity tensor in $x$ direction. Then, the viscous force of the FME in $y$ and $z$ directions can be expressed in the same way. In this regard, the viscous force of the FME is $\upsilon\nabla^2\boldsymbol{v}$. The Navier-Stokes equation in vector form is expressed as

$$\begin{cases}\dfrac{Dv}{Dt} = -\dfrac{1}{\rho}\nabla\rho + \dfrac{\mu}{\rho}\nabla^2\cdot\boldsymbol{v},\\ \nabla\cdot\boldsymbol{v} = 0.\end{cases} \tag{18}$$

In the packer test, the pressure increases slowly until it reaches the design pressure. At the same time, the time factor in Eq. (18) is ignored during the packer test. Therefore, the form of rectangular coordinate system of Eq. (18) is rewritten as

$$v_x\frac{\partial v_x}{\partial x} + v_y\frac{\partial v_x}{\partial y} = -\frac{1}{\rho}\frac{\partial p}{\partial x} + \frac{\mu}{\rho}\left(\frac{\partial^2 v_x}{\partial x^2} + \frac{\partial^2 v_x}{\partial y^2}\right), \tag{19}$$

$$v_x\frac{\partial v_y}{\partial x} + v_y\frac{\partial v_y}{\partial y} = -\frac{1}{\rho}\frac{\partial p}{\partial y} + \frac{\mu}{\rho}\left(\frac{\partial^2 v_y}{\partial x^2} + \frac{\partial^2 v_y}{\partial y^2}\right), \tag{20}$$

$$\frac{\partial v_x}{\partial x} + \frac{\partial v_y}{\partial y} = 0. \tag{21}$$

The flow of water in the two-dimensional plane rock mass fracture model is regarded as the plane one-way flow, and the initial pressure of water in the model is far greater than the dead weight of it. That is, the influence of the dead weight of water is ignored. Then,

$$\frac{\partial v_y}{\partial x} = \frac{\partial v_y}{\partial y} = 0, \tag{22}$$

$$\frac{\partial^2 v_y}{\partial x^2} = \frac{\partial^2 v_y}{\partial y^2} = 0, \tag{23}$$

$$\frac{\partial v_x}{\partial x} = \frac{\partial^2 v_x}{\partial x^2} = 0. \tag{24}$$

Substituting Eqs. (22)–(24) into Eqs. (19)–(21) yields

$$\frac{1}{\rho}\frac{\partial p}{\partial x} = \frac{\mu}{\rho}\frac{\partial^2 v_x}{\partial y^2}. \tag{25}$$

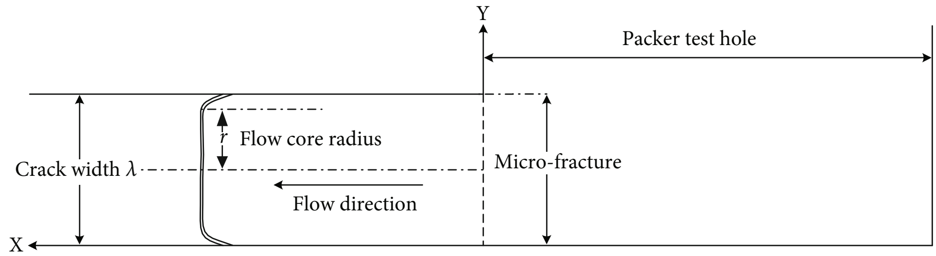


Figure 11: The structure diagram of water diffusion in microfissures.

By integrating $y$ in Eq. (25), it can be rewritten as

$$\frac{1}{\rho}\frac{\partial p}{\partial x}y + C = \frac{\mu}{\rho}\frac{\partial v_x}{\partial y}. \tag{26}$$

According to the boundary conditions of upper and lower edges of fracture, $y = r$ is the flow core radius, as shown in Figure 11. The differentiation on the right side of Eq. (26) can be expressed as:

$$\frac{\partial v_x}{\partial y} = 0, \tag{27}$$

$$C = -r\frac{\partial p}{\partial x}. \tag{28}$$

Substituting Eq. (28) into Eq. (26) yields

$$\frac{1}{\rho}\frac{\partial p}{\partial x}y - r\frac{\partial p}{\partial x} = \frac{\mu}{\rho}\frac{\partial v_x}{\partial y}. \tag{29}$$

In the constitutive equation of fluid $\tau = K\gamma^n$, the shear rate $\gamma$ is given by

$$-\frac{dv_x}{dy} = \gamma = \left(\frac{\tau}{K}\right)^{1/n}. \tag{30}$$

It is assumed that the flow of water in the fracture is not affected by external forces. If water diffuses in the form of a plane circle, the shear stress $\tau$ at the edge of the flow core radius can be expressed as

$$\tau = -\frac{y}{2}\frac{dp}{dx}, \tag{31}$$

where negative sign represents flow direction. Then, substituting Eq. (30) and Eq. (31) into Eq. (29), change rate of pressure gradient is expressed as follows:

$$\frac{dp}{dx} = \left(\frac{y\mu^n}{2K(y-\rho r)^n}\right)^{1/(n-1)}. \tag{32}$$

The packer test hole radius is expressed as $x = r_0$, and the initial pressure of water is expressed as $p = p_0$. Eq. (32) is integrated based on the expansion of boundary conditions and initial conditions, and we obtain the following:

$$\triangle p = p_0 - p_x = \left(\frac{y\mu^n}{2K(y-\rho r)^n}\right)^{1/(n-1)}(x - r_0). \tag{33}$$

According to the hypothesis of effective stress, the total stress of the fluid-solid coupling system formed by water and rock mass can be regarded as the sum of water pressure and equivalent stress of rock mass. However, the rock block in the actual engineering is fixed by surrounding rock mass. For the three-dimensional state of the fracture network, it is projected into a two-dimensional fracture network, where each rock block is always set with one fixed boundary. It ensures that rock blocks do not rotate due to fluid pressure. Therefore, the pressure at the fluid boundary is equal to the pressure at the fracture boundary.

$$P_1 = P_2 = -\mathbf{n}\cdot\left(-p\mathbf{I} + \mu\left(\nabla\mathbf{v} + (\nabla\mathbf{v})^T\right)\right), \tag{34}$$

where $P_1$ represents the fluid pressure at fluid boundary, $P_2$ represents the equivalent stress at fracture surface, $\mathbf{n}$ is the normal tensor direction of boundary interface, $\mathbf{I}$ represents the unit tensor, $\mathbf{v}$ represents the velocity tensor.

*4.3. Diffusion Characteristics.* In the simulation, the following assumptions are made:

(1) Water is an incompressible fluid

(2) The permeability of the rock block is 0. That is, liquid will not penetrate the rock block but will flow and diffuse along the fracture

(3) The influence of fluid-solid coupling between water and rock blocks on water diffusion is ignored

In Table 3, the fractal dimension of the current study is 1.79. Barton and Zoback [39] reported that the fluctuation range, the fractal dimension of 2D maps of the fracture length, is 1.3 to 1.7. In this paper, the research object is broken rock mass. The fracture network formed by the broken rock mass is a connected open fracture. Thus, the fractal dimension value 1.79 is beyond the range 1.3 to 1.7 given in the literature [39]. It hints that the current fractal dimension value of 1.79 is reasonable.

Under an initial pressure of 0.8 MPa, the diffusion of water in the plane model is shown in Figures 12 and 13. Figure 12 shows the distribution of water diffusion pressure in the fracture network, and Figure 13 shows the

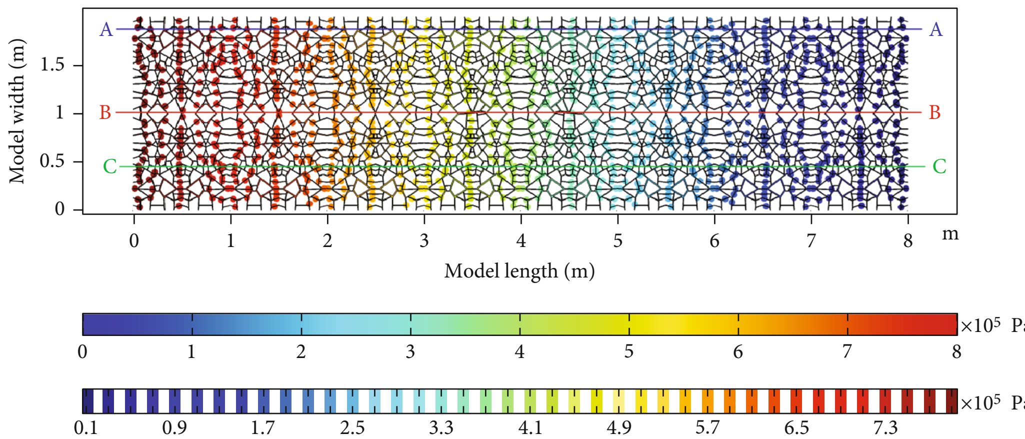


Figure 12: Variation trend of water diffusion pressure (No. A).

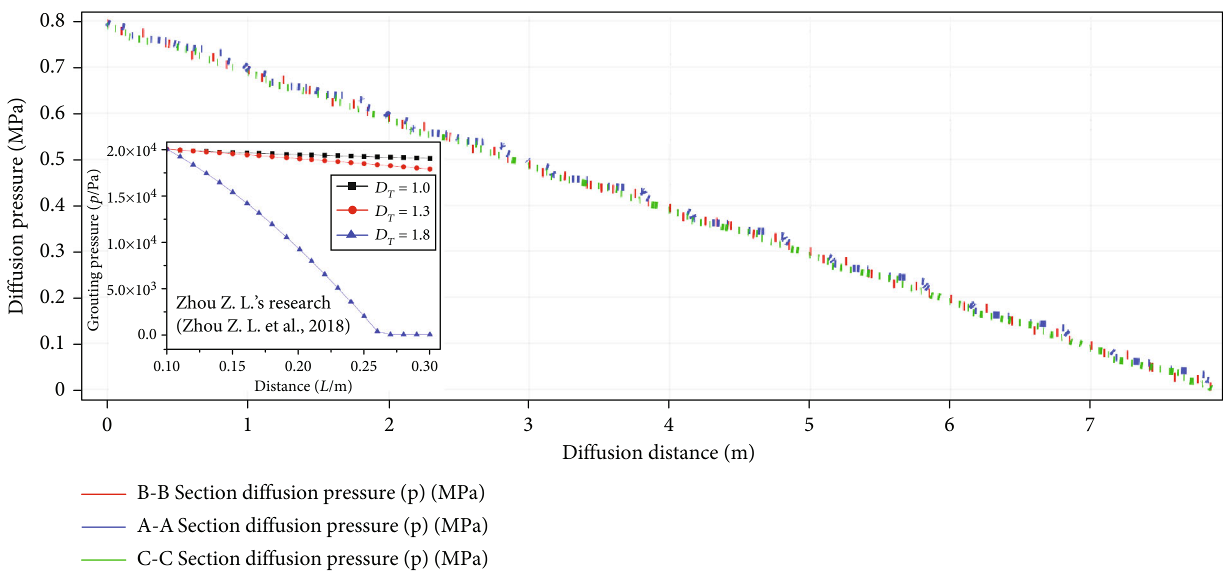


Figure 13: Distribution characteristics of water pressure with diffusion distance (No. A).

variation trend of water diffusion pressure in sections A-A, B-B, and C-C.

Figure 13 reveals a relationship between fluid diffusion pressure and diffusion distance in the fracture model. It is shown from Figure 13 that the flow diffusion pressure in the fracture network is approximately linear. When the water diffuses, the pressure distribution shows different states with an irregular distribution of fractures. In the model, the diffusion pressure shows good consistency along a symmetrical measurement line, suggesting that the irregular distribution of fractures greatly influences the distribution of water pressure in the fracture network. In contrast, the irregular distribution of fractures has little effect on the initial inlet pressure and outlet end pressure of the packer test.

Lines A-A, B-B, and C-C of Figure 12 correspond to the centerline area, the upper edge area, and dense fractures in the model, respectively. Figure 13 shows that in the process of water diffusion, the diffusion pressure varies with the diffusion distance in sections A-A, B-B, and C-C of Figure 12. Figure 13 indicates that the diffusion pressure of water linearly decreases with diffusion distance. This study shows that in the water pressure experiment of a broken rock mass, the diffusion pressure of water decreases linearly along the diffusion direction in the whole packer test section.

Figure 14 shows that two mainstream channels are formed in the fracture network, and the mainstream channels appear in the region where the fractures are sparsely distributed. The fracture orientation approximately consistent with the diffusion direction has a high flow velocity and is called the horizontal mainstream channel. In Figure 14, the region between line I and line II is horizontal mainstream channel (HMC). In the area with considerable fragmentation, the diffusion velocity of water is very high. In contrast, the water diffusion velocity of the sparse region is relatively low. Additionally, it can be concluded from Figure 14 that the flow diffusion velocity in the fracture consistent with the diffusion direction is significantly higher than the flow diffusion velocity in other fractures.

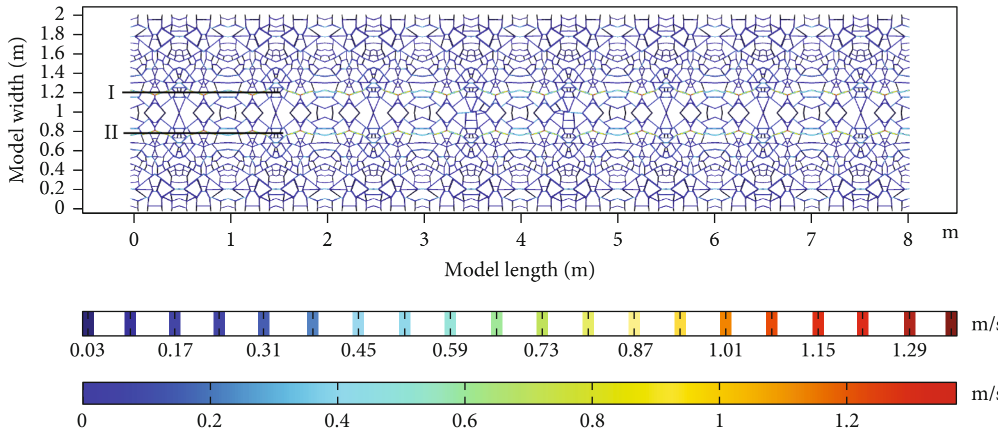


Figure 14: Distribution characteristics of water flow diffusion velocity in the fracture network (No. A).

It can be concluded from Figure 14 that regarding the connected fracture network structure of the broken rock mass, the distribution of the fracture network plays a crucial role in controlling the diffusion rate of water. In the area with densely distributed fractures and a small fracture width, the diffusion velocity of water is low. In an area with sparsely distributed fractures and a large fracture width, the diffusion velocity of water is very high. When a mainstream channel is formed, the diffusion velocity of water in this fracture is greater than the diffusion velocity of water in other fractures.

The four random fractures are used to display diffusion velocity to reader, as shown in Figure 15. The velocity distribution in each fracture is approximately symmetrical. The diffusion velocity within the radius flow core is the highest, and the velocity near the fracture wall decreases linearly. Thus, it can be concluded that the water diffusion velocity in fracture can be regarded as a composite plate Poisson flow.

According to fracture parameters in Table 3, various two-dimensional plane models are established to simulate the diffusion state of water in fractures. Because the fractal dimension is consistent, the simulation results display a similarity for the diffusion velocity nephogram of various model. Thus, four parameters, such as diffusion velocities $v_{\max}$ and $v_{\min}$, maximum fracture flow channel (Max-CFC), and minimum fracture flow channel (Min-CFC), are used to characterize the diffusion differences of water in different models. Then, the distribution characteristics of the water diffusion velocity in fractures are shown in Figure 16.

In the corresponding models from No. A to No. F, the diffusion velocities of the minimum fractures are 0.402 m/s, 0.432 m/s, 0.49 m/s, 0.427 m/s, 0.441 m/s, and 0.54 m/s, respectively. In similar, the diffusion velocities of the maximum fractures are 0.356 m/s, 0.263 m/s, 0.485 m/s, 0.275 m/s, 0.313 m/s, and 0.562 m/s, respectively. The above velocity values exhibit randomness and disorder. This indicates that the single factor, the maximum fracture width, has little effect on the diffusion rate of water in the entire fracture network.

In Figure 16, the maximum values $v_{\max}$ corresponding to No. A to No. F are 1.297 m/s, 1.412 m/s, 1.3 m/s, 1.317 m/s, 1.42 m/s, and 1.341 m/s, respectively, and the minimum values $v_{\max}$ are 0.126 m/s, 0.163 m/s, 0.078 m/s, 0.203 m/s, 0.163 m/s, and 182 m/s, respectively. Despite the diffusion velocities $v_{\max}$ and $v_{\min}$ barely exhibit regularity, the ratio of mean velocity to maximum velocity is less than 0.5, which also indicates laminar flow.

Figure 16 indicates that the maximum value and minimum value of diffusion velocity have nothing to do with Max-CFC and Min-CFC in fracture network model. Also, it can be concluded from Figure 16 that the distribution of Max-CFC and Min-CFC has little impact on the maximum and minimum velocities of the entire fracture model. To explore the characteristics of water diffusion velocity in fracture networks, a single fracture network model was constructed to reveal the diffusion characteristics of water, as shown in Figure 17. In Figure 17, $v$ represents the flow velocity, and $\sigma_v$ represents the volume stress generated by the fluid velocity on the solid boundary.

When the initial pressure is constant, the diffusion velocity decreases with increasing fracture width, as shown in fracture channel 1 and fracture channel 2 of Figure 17. Then, fracture channel 1 is divided into fracture channel 3 and fracture channel 4 resulting in a clear decrease of the diffusion velocity of them. The diffusion velocity of fracture channel 4 is significantly lower than that of fracture channel 3. There are two main reasons: one is the width of the fracture, and the other is shown in Figure 18(a), which is energy cancellation between the velocity components $v_{1y}$ and $v_{2y}$. In addition, Figure 18(b) shows the alternative type energy cancellation and the energy superposition, which are $v_{4y} - v_{5y}$ and $v_{4x} + v_{5x}$, respectively. In Figure 18, $v_{1y}$ represents velocity component of fracture channel 1 exit in $y$ direction, and $v_{1x}$ represents velocity component of fracture channel 1 exit in $x$ direction. The other symbols of Figure 18 can be deduced according to the above rules.

For fracture channel 5 of Figure 17, the diffusion velocity is the maximum value. The critical reason is that the diffusion energy of fracture channel 2 is mainly transmitted through fracture channel 5 and the width of fracture channel 5 decreases compared to fracture channel 2. In fracture

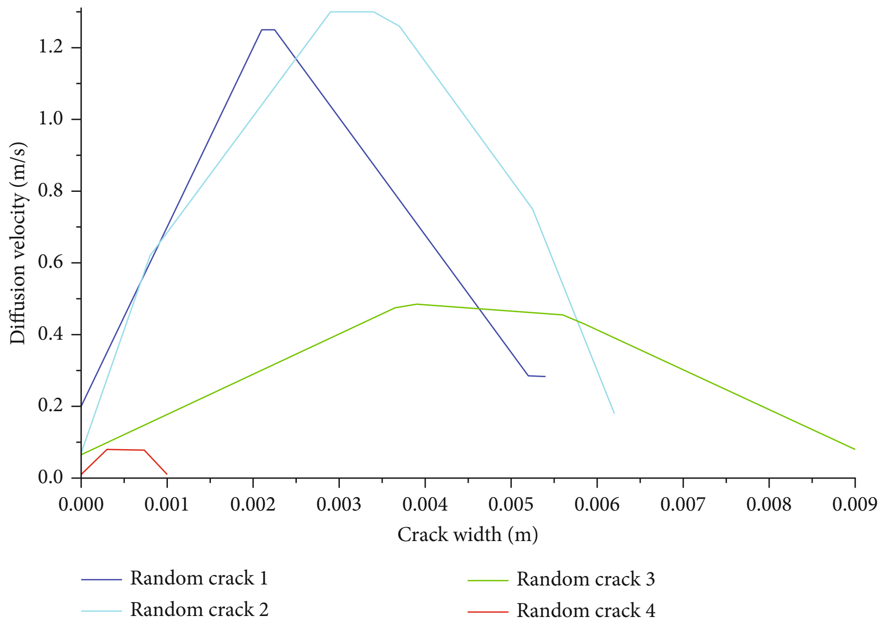


Figure 15: The water flow diffusion velocity of the random fracture.

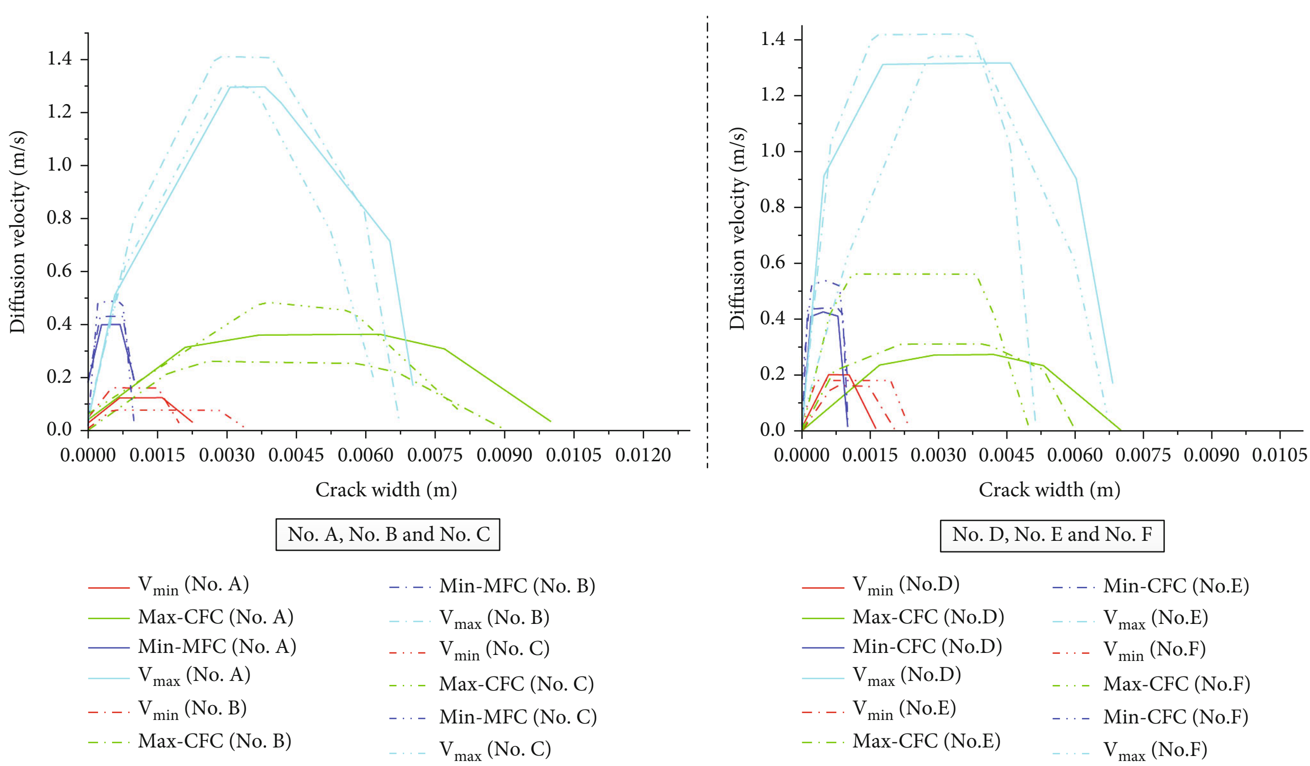


Figure 16: The water flow diffusion velocity of the critical fracture.

channel 8 of Figure 17, a backflow phenomenon is displayed when $v_{3y}$ is much greater than $v_{4y}$. Thus, it is possible to show the minimum diffusion velocity in fracture channel 8 of Figure 17. Of course, the maximum diffusion velocity may be displayed on a fracture channel, such as the fracture channel with $v_{4x} + v_{5x}$ status in Figure 18(b).

## 5. Results and Discussion

In this section, the two-dimensional fracture network model predictions will be compared with experimental data and diffusion velocity will be discussed. The determination of relevant parameters for modeling procedures in Figure 5 is as follows:

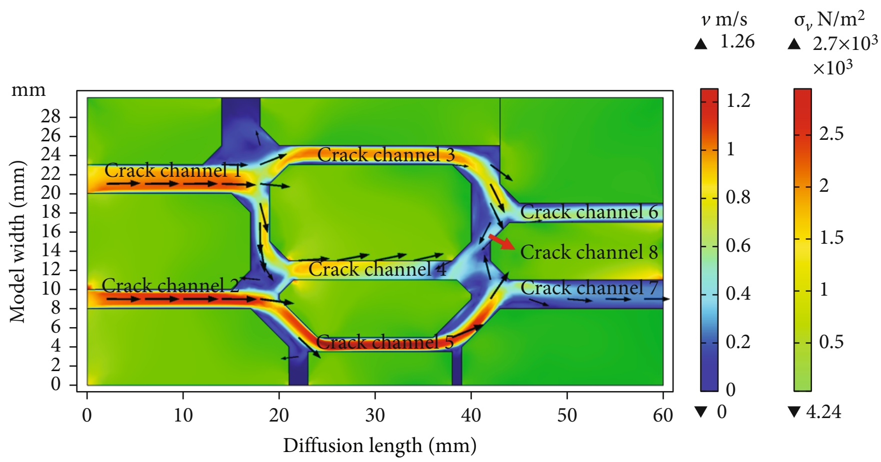


Figure 17: Diffusion characteristics of water flow in a single fracture network.


(a) Offset mode of diffusion velocity in the $y$ direction (b) The superposition mode of diffusion velocity in the $x$ direction

Figure 18: Schematic diagram of energy dissipation at the intersection of fractures.

(1) Given the fracture network of a broken rock mass based on a real underground mine, the Fankou Lead-Zinc Mine

(2) Determine the fractal dimension $D_f$ of fracture width in a two-dimensional fracture network model by Eq. (5)

(3) The permeability determination for broken rocks is carried out in packer test and empirical relationship by Eq. (9) and Eq. (10)

(4) Infer the porosity $\phi_a$ of fractures by Eq. (12)

(5) List the fracture widths $\lambda_{min}$ and $\lambda_{max}$ by Table 3

(6) Construct the two-dimensional fracture network model by Figure 8

(7) Finally, simulate the diffusion property by Section 4

The previous fractal property for length distribution of fractures [19] has been proposed. It is concluded that the permeability of fractured rocks is a function with fracture characteristic parameters, such as the fractal dimension $D_f$, fracture density, the facture azimuth, facture dip angle, and fracture aperture. In comparison, the two-dimensional fracture network model of broken rock mass is modeled and simulated by Sections 3 and 4, respectively. Figure 14 shows that the current model simulations agree well with the experimental results [4]. Miao et al. [19] proposed that the permeability decreases with porosity. Similarly, it can be seen from Figure 14 that an area with higher fracture density has lower diffusion. Also, the current simulation prediction is consistent with practical situation. In Figure 18, the high dip angle of fracture leads to a decrease horizontal component for flow velocity. Thus, it is concluded from Figure 18 that a high dip angle is also resistant for fluid flow. This coincides with Miao et al.'s research [19]. Besides, Figure 13 shows that the current simulations are approximate to the existing test and derivation results when $D_f = 1.8$ [4].

In this research, the fracture randomness in the fracture model unit has not been qualitatively described. Instead, the fracture model unit is generated on the basis of satisfying the maximum crack width, minimum crack width, and fractal dimension. Although there is a certain difference between the fracture model unit and the actual fracture state, the fractal dimension exhibited by the fracture model unit is consistent with the actual packer test. Thus, this study has assuredly reference value for guiding practical engineering.

## 6. Conclusions

In the current research, the packer test is applied to determine permeable rate, and the empirical relationship between osmotic coefficient and fractal dimension is stated. Then, the fractal geometry theory is used to describe the fracture system of broken rock mass, and fractal dimension for width distribution of fractures has been proposed. Based on the above, a two-dimensional fracture network model is generated by the symmetrical expansion method for the model unit. Through simulation analysis and comparative verification of the current model, we give some of following conclusions:

(1) The diffusion velocity of fracture networks decreases with increasing fracture density and dip angle

(2) The diffusion velocities $v_{\min}$ and $v_{\max}$ are not much to do with the fracture widths $\lambda_{\min}$ and $\lambda_{\max}$ in the entire fracture network. The diffusion velocity of fracture model is more affected by the density and horizontal inclination of fractures

(3) The simulation has verified the feasibility of using crack width to construct a two-dimensional plane fracture network model for fractured rock masses

(4) The fracture width is an absolute critical factor for the diffusion velocity of a single fracture. Our simulations are concordant with available research results. This indicates that the proposed modeling method is reliable

In addition, it should be pointed out that we focus on modeling broken rock mass. It is assumed that all fractures are connected to form an interconnected fracture network. Compared to existing researches, a definite advantage of the current predictions is that the fluid-solid coupling of the model displays the interaction between fractures. However, the quantitative description of fracture randomness on the entire fracture network system has been ignored. The quantitative analysis of fracture dip angle was not carried out in this study. These are interesting subdomains and will be our next research.

## Data Availability

The data used to support the findings of this study are included within the article.

## Conflicts of Interest

The authors declare that they have no known competing financial interests or personal relationships that could have appeared to influence the work reported in this paper.

## Acknowledgments

The authors are grateful to the Chongqing Postdoctoral Science Foundation (Grant No. cstc2021jcyj-bshX0032), the Scientific and Technological Innovation Team of Chongqing Industry Polytechnic College, and the science and technology research project of Chongqing Education Commission of China (Grant No. KJQN202003208), for supporting this research. This study is also supported by the Doctoral Fund of Chongqing Industry Polytechnic College (Grant No. 2023GZYBSZK1-12), Natural Science Foundation of Chongqing (Grant No. cstc2021jcyj-msxmX0959), and youth project of science and technology research program of Chongqing Education Commission of China (Grant No. KJQN202203226).

## References

[1] H. Güllü, "Factorial experimental approach for effective dosage rate of stabilizer: application for fine-grained soil treated with bottom ash," *Soils and Foundations*, vol. 54, no. 3, pp. 462–477, 2014.

[2] S. C. Li, R. T. Liu, Q. S. Zhang, and X. Zhang, "Protection against water or mud inrush in tunnels by grouting: a review," *Journal of Rock Mechanics and Geotechnical Engineering*, vol. 8, no. 5, pp. 753–766, 2016.

[3] S. Saleh, N. Z. M. Yunus, K. Ahmad, and N. Ali, "Improving the strength of weak soil using polyurethane grouts: a review," *Construction and Building Materials*, vol. 202, no. 6, pp. 738–752, 2019.

[4] Z. L. Zhou, X. M. Du, S. Y. Wang, and H. Z. Zang, "Analysis and engineering application investigation of multiple-hole grouting injections into porous media considering filtration effects," *Construction and Building Materials*, vol. 186, pp. 871–883, 2018.

[5] C. Y. Xie, H. Nguyen, X. N. Bui, V. T. Nguygn, and J. Zhou, "Predicting roof displacement of roadways in underground coal mines using adaptive neuro-fuzzy inference system optimized by various physics-based optimization algorithms," *Journal of Rock Mechanics and Geotechnical Engineering*, vol. 13, no. 6, pp. 1452–1465, 2021.

[6] C. Y. Xie, H. Nguyen, C. Yosoon, and D. J. Armaghani, "Optimized functional linked neural network for predicting diaphragm wall deflection induced by braced excavations in clays," *Geoscience Frontiers*, vol. 13, no. 2, article 101313, 2022.

[7] J. Alireza and B. Tayfun, "Effective fracture network permeability of geothermal reservoirs," *Geothermics*, vol. 40, no. 1, pp. 25–38, 2011.

[8] J. J. Andrade, E. Oliveira, A. Moreira, and H. J. Herrmann, "Fracturing the optimal paths," *Physical Review Letters*, vol. 103, no. 22, article 225503, 2009.

[9] E. Bonnet, O. Bour, N. E. Odling et al., "Scaling of fracture systems in geological media," *Reviews of Geophysics*, vol. 39, no. 3, pp. 347–383, 2001.

[10] M. Sahimi, "Flow phenomena in rocks: from continuum models to fractals, percolation, cellular automata, and simulated annealing," *Reviews of Modern Physics*, vol. 65, no. 4, pp. 1393–1534, 1993.

[11] K. Watanabe and H. Takahashi, "Fractal geometry characterization of geothermal reservoir fracture networks," *Journal of Geophysical Research: Solid Earth*, vol. 100, no. B1, pp. 521–528, 1995.

[12] M. Y. Wu, D. M. Zhang, W. S. Wang et al., "Numerical simulation of hydraulic fracturing based on two-dimensional surface fracture morphology reconstruction and combined finite-discrete element method," *Journal of Natural Gas Science and Engineering*, vol. 82, article 103479, 2020.

[13] M. Y. Wu, W. S. Wang, D. Shi, Z. L. Song, M. H. Li, and Y. F. Luo, "Improved box-counting methods to directly estimate the fractal dimension of a rough surface," *Measurement*, vol. 177, no. 1, article 109303, 2021.

[14] A. Torabi and S. S. Berg, "Scaling of fault attributes: a review," *Marine and Petroleum Geology*, vol. 28, no. 8, pp. 1444–1460, 2011.

[15] B. Velde, J. Dubois, D. Moore, and G. Touchard, "Fractal patterns of fractures in granites," *Earth and Planetary Science Letters*, vol. 104, no. 1, pp. 25–35, 1991.

[16] M. Vignes-Adler, A. Le Page, and P. M. Adler, “Fractal analysis of fracturing in two African regions, from satellite imagery to ground scale,” *Tectonophysics*, vol. 196, no. 1-2, pp. 69–86, 1991.

[17] M. Y. Wang, J. S. Chen, and L. Wan, “Application of stochastic fracture network with numerical fluid flow simulations to groundwater flow modeling in fractured rocks,” *Journal of China University of Geosciences*, vol. 12, no. 3, pp. 240–248, 2001.

[18] Q. Zheng and B. Yu, “A fractal permeability model for gas flow through dual-porosity media,” *Journal of Applied Physics*, vol. 111, no. 2, pp. 024316–0243167, 2012.

[19] T. J. Miao, B. M. Yu, Y. G. Duan, and Q. G. Fang, “A fractal analysis of permeability for fractured rocks,” *International Journal of Heat and Mass Transfer*, vol. 81, pp. 75–80, 2015.

[20] J. S. Lee, C. S. Bang, Y. J. Mok, and S. H. Joh, “Numerical and experimental analysis of penetration grouting in jointed rock masses,” *International Journal of Rock Mechanics and Mining Sciences*, vol. 37, no. 7, pp. 1027–1037, 2000.

[21] G. Lombardi, “Grouting of rock masses,” in *Grouting and Ground Treatment*, vol. 120, no. 1pp. 164–197, Proceedings of the third international conference, Geotechnical Special Publication, 2003.

[22] M. E. Tani, “Grouting rock fractures with cement grout,” *Rock Mechanics and Rock Engineering*, vol. 45, no. 4, pp. 547–561, 2012.

[23] W. S. Wang, G. S. Cao, Y. Li et al., “Experimental study of dynamic characteristics of tailings with different reconsolidation degrees after liquefaction,” *Frontiers in Earth Science*, vol. 10, article 876401, 2022.

[24] L. Wen, Z. Q. Luo, Y. G. Qin, and Z. Y. Luo, “The use of Hoek Brown failure criterion on determination of the geomechanical parameters of a grouting consolidation body,” *IEEE Access*, vol. 7, no. 1, pp. 142703–142714, 2019.

[25] K. Lange and P. J. Van Geel, “Physical and numerical modelling of dual-porosity fractured rock surrounding an in-pit uranium tailings management facility,” *Canadian Geotechnical Journal*, vol. 48, no. 3, pp. 365–374, 2011.

[26] S. Nishimura, K. Takehana, Y. Morikawa, and H. Takahashi, “Experimental study of stress changes due to compaction grouting,” *Soils and Foundation*, vol. 51, no. 6, pp. 1037–1049, 2011.

[27] X. M. Du, H. Y. Fang, S. Y. Wang, B. H. Xue, and F. M. Wang, “Experimental and practical investigation of the sealing efficiency of cement grouting in tortuous fractures with flowing water,” *Tunnelling and Underground Space Technology*, vol. 108, article 103693, 2021.

[28] S. Kvartsberg and A. Fransson, “Hydrogeological characterisation and stochastic modelling of a hydraulically conductive fracture system affected by grouting: a case study of horizontal circular drifts,” *Tunnelling and Underground Space Technology*, vol. 38, pp. 38–49, 2013.

[29] H. Zhou, M. Xiao, and J. T. Chen, “Analysis of a numerical simulation method of fully grouted and anti-seismic support bolts in underground geotechnical engineering,” *Computers and Geotechnics*, vol. 76, pp. 61–74, 2016.

[30] Q. H. Lei, X. G. Wang, K. B. Min, and J. Rutqvist, “Interactive roles of geometrical distribution and geomechanical deformation of fracture networks in fluid flow through fractured geological media,” *Journal of Rock Mechanics and Geotechnical Engineering*, vol. 12, no. 4, pp. 780–792, 2020.

[31] National Development and Reform Commission of the people's Republic of China, “Technical code for high pressure jet grouting of water conservancy and hydropower projects,” P-DL/T5200-2004.

[32] J. Z. Wu, *The Study of Correlation between Permeability and Fractal Dimension of Porous Media*, Chinese, 2015.

[33] C. Klimczak, R. A. Schultz, R. Parashar, and D. M. Reeves, “Cubic law with aperture-length correlation: implications for network scale fluid flow,” *Hydrogeology Journal*, vol. 18, no. 4, pp. 851–862, 2010.

[34] J. H. Kruhl, “Fractal-geometry techniques in the quantification of complex rock structures: a special view on scaling regimes, inhomogeneity and anisotropy,” *Journal of Structural Geology*, vol. 46, pp. 2–21, 2013.

[35] R. A. Schultz, R. Soliva, H. Fossen, C. H. Okubo, and D. M. Reeves, “Dependence of displacement-length scaling relations for fractures and deformation bands on the volumetric changes across them,” *Journal of Structural Geology*, vol. 30, no. 11, pp. 1405–1411, 2008.

[36] B. M. Yu and J. H. Li, “Some fractal characters of porous media,” *Fractals*, vol. 9, no. 3, pp. 365–372, 2001.

[37] J. Z. Qian, Z. Chen, H. B. Zhan, and H. C. Guan, “Experimental study of the effect of roughness and Reynolds number on fluid flow in rough-walled single fractures: a check of local cubic law,” *Hydrological Processes*, vol. 25, no. 4, pp. 614–622, 2011.

[38] K. P. Travis and K. E. Gubbins, “Poiseuille flow of Lennard-Jones fluids in narrow slit pores,” *The Journal of Chemical Physics*, vol. 112, no. 4, pp. 1984–1994, 2000.

[39] C. A. Barton and M. D. Zoback, “Self-similar distribution and properties of macroscopic fractures at depth in crystalline rock in the Cajon pass scientific drill hole,” *Journal of Geophysical Research: Solid Earth*, vol. 97, no. B4, pp. 5181–5200, 1992.